Bioactive Materials 6 (2021) 2956–2968

Contents lists available at ScienceDirect

Bioactive Materials

journal homepage: www.sciencedirect.com/journal/bioactive-materials

Erythrocyte membrane-camouflaged nanoworms with on-demand antibiotic release for eradicating biofilms using near-infrared irradiation

Luoxiao Ran [a,1], Bitao Lu [a,1], Haoyu Qiu [a], Guofang Zhou [a], Jing Jiang [c], Enling Hu [a,b], Fangyin Dai [a,b], Guangqian Lan [a,b,*]

[a] State Key Laboratory of Silkworm Genome Biology, College of Sericulture, Textile and Biomass Sciences, Southwest University, Chongqing, 400715, China
[b] Chongqing Engineering Research Center of Biomaterial Fiber and Modern Textile, Chongqing, 400715, China
[c] Chongqing General Hospital, University of Chinese Academy of Sciences No.118, Xingguang Avenue, Liangjiang New Area, Chongqing, China

ARTICLE INFO

Keywords:
Red blood cell membrane
Nanoworms
Antibiotics release
Bacterial infection

ABSTRACT

The increase in the number of resistant bacteria caused by the abuse of antibiotics and the emergence of biofilms significantly reduce the effectiveness of antibiotics. Bacterial infections are detrimental to our life and health. To reduce the abuse of antibiotics and treat biofilm-related bacterial infections, a biomimetic nano-antibacterial system, RBCM-NW-G namely, that controls the release of antibiotics through near infrared was prepared. The hollow porous structure and the high surface activity of nanoworms are used to realize antibiotic loading, and then, biomimetics are applied with red blood cell membranes (RBCM). RBCM-NW-G, which retains the performance of RBCM, shows enhanced permeability and retention effects. Fluorescence imaging in mice showed the effective accumulation of RBCM-NW-G at the site of infection. In addition, the biomimetic nanoparticles showed a longer blood circulation time and good biocompatibility. Anti-biofilm test results showed damage to biofilms due to a photothermal effect and a highly efficient antibacterial performance under the synergy of the photothermal effect, silver iron, and antibiotics. Finally, by constructing a mouse infection model, the great potential of RBCM-NW-G in the treatment of in vivo infections was confirmed.

1. Introduction

Bacterial infection is a common clinical disease that threatens people's health and even life [1,2]. In the past few decades, the emergence of antibiotics has enabled the effective treatment of bacterial infections [3]. However, antibiotic-resistant bacteria have been increasing due to the abuse of antibiotics [4]. In addition, the formation of biofilms hinders the penetration of antibiotics and inactivates them, thereby further increasing the resistance of bacteria [5,6]. Therefore, bacterial infections are becoming even more dangerous [7]. Ten million people worldwide are expected to die from drug-resistant bacterial infections by 2050 [8]. Although researchers have developed many new antibacterial strategies, antibiotic treatment is still the most commonly used method in clinical practice [9]. Therefore, there is an urgent need to develop new antibacterial strategies and use antibiotics more efficiently.

Among these new strategies, topical antibiotic use is a feasible one. Local use of antibiotics, instead of systemic use, can effectively reduce the risk of drug-resistance development [10]. The topical use of antibiotics generally includes the use of a carrier to transport the antibiotics to the infected site to achieve a more efficient use [11]. In addition, photothermal therapy (PT) has received widespread attention because it can be controlled remotely and is not affected by the microenvironment [12,13]. PT refers to the use of photothermal materials to rapidly convert light energy into heat under the excitation of near-infrared light [14]. Therefore, local heating can be used to lyse bacteria so that they do not develop resistance [15,16]. However, high temperatures cause damage to surrounding tissues, while low temperatures do not have an ideal sterilization effect [17]. Therefore, a combined antibacterial strategy comprising antibiotic therapy and PT is an effective solution [18].

The unique optical properties of gold-silver alloy nanoparticles (AuAg) make it widely used in PT [19,20]. In addition to its photothermal effect, AuAg has a hollow inside and is porous outside, a

Peer review under responsibility of KeAi Communications Co., Ltd.
* Corresponding author. State Key Laboratory of Silkworm Genome Biology, College of Sericulture, Textile and Biomass Sciences, Southwest University, Chongqing, 400715, China.
E-mail address: j070218@swu.edu.cn (G. Lan).
[1] These authors are contributed equally to this work.

https://doi.org/10.1016/j.bioactmat.2021.01.032
Received 17 November 2020; Received in revised form 7 January 2021; Accepted 28 January 2021

structure suitable for loading drugs; therefore, it is widely used in tumor treatment [21]. Moreover, AuAg can be used as an antibacterial agent alone because it can release a broad-spectrum of antibacterial agent Ag ions [3]. Therefore, using AuAg as an antibiotic carrier and PT for synergistic sterilization is expected to improve the antibacterial effect. However, the ideal antibiotic carrier should have a high drug loading efficiency, while AuAg alone has a limited loading efficiency [22]. Polydopamine (PDA) is widely used in the biomedical field owing to its good biocompatibility and degradability [23,24]. More importantly, PDA can adsorb drugs via π−π stacking and/or hydrogen bonding interactions and can be released under near-infrared light excitation [25,26].

Furthermore, these drug-loaded materials are often cleared quickly by the immune system, which significantly reduces the efficiency of drug delivery [27,28]. Enabling nanocarriers to escape the immune system and prolonging the circulation time in the body to effectively use antibiotics is another aspect of alleviating bacterial resistance [29,30]. In recent years, macrophage membranes [31], platelet membranes [32], red blood cell membranes (RBCMs) [33], and stem cell membranes [34] have widely been used in nanoparticle biominimization to avoid clearance by the immune system. Among them, RBCMs have many immunomodulatory markers, so that their use to camouflage the nanoparticles can increase the circulation time of these particles in the body [35,36]. The enhanced permeability and permeability and retention (EPR) effect due to RBCMs, results in an accumulation of the nanoparticles at the site of infection [37,38].

Herein, a combined antibacterial strategy to provide a new method for the rational use of antibiotics is proposed. As shown in Fig. 1, AuAg is used as a carrier to store the typical antibiotic gentamicin (GM), forming GM filled AuAg (AuAg-G); next, dopamine self-aggregation is used to form a PDA coating to wrap AuAg, forming PDA wrapped AuAg-G. As PDA wrapping AuAg could form a nanoworm (NW) particle, PDA wrapped AuAg-G was thus denoted as NW-G. During dopamine self-aggregation over AuAg-G, some GM may also be adsorbed to PDA surface, leading to improved loading efficiency. Finally, NW-G is encapsulated with RBCM, forming RBCM-camouflaged NW-G (RBCM-NW-G), to increase its blood circulation time and induce an effective accumulation at the infected site. Finally, NIR excitation is used at the infected site. Through the photothermal effect of AuAg and PDA, GM and Ag ions (Ag^+) are released to realize the synergistic sterilization of antibiotics. Therefore, the proposed method reduces the risk of death from bacterial infection and the economic burden for the healthcare system, thus delaying the occurrence of antibiotic resistances.

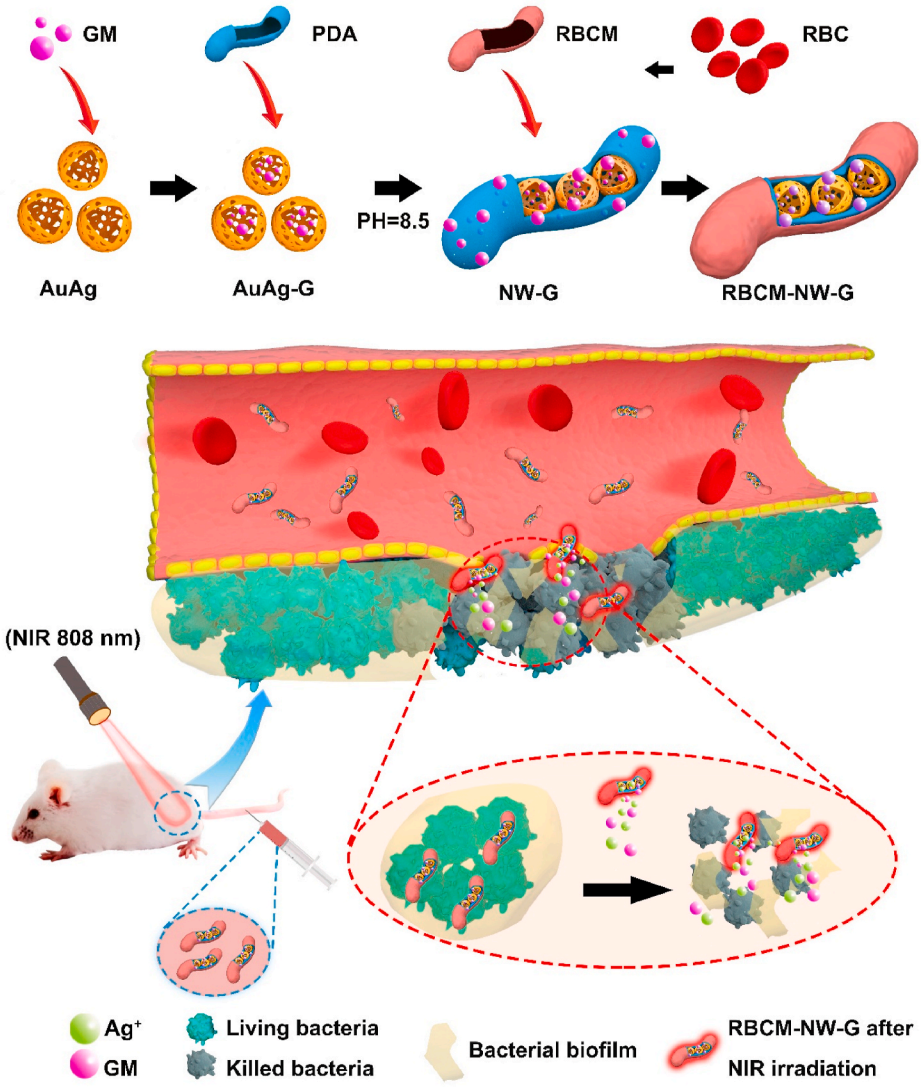

Fig. 1. Diagram of RBCM-NW-G preparation and the treatment principle of bacterial infections in vivo.

2. Experimental

2.1. Preparation of silver nanoparticles (AgNPs)

Tannic acid (0.25 g) was firstly added to boiling deionized (DI) water (100 mL) under stirring (600 rpm/min). Then, silver nitrate solution (2 wt %, 1 mL) was added in the above solution; stirring was continued until the color of solution turned to yellow-green, after which the resultant mixture was placed in ice-water bath (0 °C) for cooling. Then the resultant particles (AgNPs) from the mixture were isolated by centrifugation (10,000 r/min, 10 min), and washed three times to remove impurities. Finally, AgNPs were re-dispersed in DI water (30 mL) and kept in a refrigerator (4 °C) for subsequent use.

2.2. Preparation of AuAg

AgNPs dispersion (5 mL) prepared above was added to DI water (25 mL), which was then heated to boil under stirring (600 r/min) on a hot plate. Then, chloroauric acid solution (0.8 mM) was added to the above solution dropwise at an ultralow dosing rate at 20 mL/h. With the addition of chloroauric acid, the color of the solution gradually turned blue (Fig. S1A). During this period, the UV absorption profile of the blue solution was examined dynamically; when the maximum absorption wavelength shifted to approximately 750 nm, the reaction was terminated immediately and the solution was placed in ice water for cooling. Then ammonia solution (200 μL) was added into the blue mixture to dissolve the silver chloride precipitate. The resultant mixture was then centrifugated (10,000 r/min, 10 min) to isolate AuAg, which was then washed three times, before it was re-dispersed in DI water again (3 mg/mL). The dispersion was then stored in a refrigerator (4 °C) for later use.

2.3. Preparation of RBCM

The RBCM was derived from the blood of female BALB/c mice. Briefly, ethylenediaminetetraacetic acid (EDTA) (15 mg) was added to the freshly drawn whole blood (10 mL), which were then centrifuged (3000 rpm, 5 min) at 4 °C to isolate RBCM. After washed three times with phosphate-buffered saline containing disodium ethylenediaminetetraacetate dihydrate (1 mM) (PBS-EDTA-Na_2) at 4 °C, RBCM was socked with diluted PBS-EDTA-Na_2 (4-fold) at 4 °C for 30 min. Finally, the RBCM was separated by centrifugation (4 °C, 14,000 rpm, 5 min), and then washed with PBS-EDTA-Na_2 (4 °C) thoroughly. All the yielded RBCM from whole blood (10 mL) was then stored in PBS-EDTA-Na_2 (10 mL) in a refrigerator (4 °C) for subsequent use.

2.4. Preparation of AuAg-G and NW-G

GM (2.0 mg) was firstly filled into AuAg, before AuAg was wrapped with PDA, following a loading-before-wrapping protocol. Specifically, GM was pre-dissolved in Tris solution (5 mM, 5 mL), which was then mixed with AuAg dispersion (1 mg/mL, 5 mL) under sonication to obtain AuAg-G. After sonication for another 15 min, PDA (0.005 g) pre-dissolved in Tris solution (2.5 mM, 10 mL) was added in the mixture to wrap AuAg-G for preparation of NW-G (GM may also be adsorbed by the surface of PDA simultaneously). After continuous stirring under ultrasound for 1 h, NW-G were centrifugated (8000 r/min, 5 min) and washed with DI water three times. After drying at 60 °C for 4 h, NW-G was ready for use.

2.5. Encapsulation of RBCM over NW-G and NW-g

NW-G and NW-g dispersions (0.2 mg/mL, 5 mL) were mixed with 10-fold diluted RBCM dispersion (1 mL) prepared in Section 2.3, and ultrasonicated for 5 min to allow encapsulation, forming RBCM-NW-G and RBCM-NW-g. The photographs of Ag, AuAg, NW-G, and RBCM-NW-G are shown in Fig. S1B.

2.6. Characterization

Transmission electron microscopy (TEM Talos F200X) and high-angle annular dark-field imaging-scanning transmission electron microscopy (HAADF-STEM) were used to observe the particle, and map typical elements by energy-dispersive X-ray spectroscopy (EDS). UV–vis spectra were detected using a UV spectrophotometer. The potential and size of the particles were determined using a Zetasizer Nano ZS (Malvern, UK). Sodium salt-Polyacrylamide gel electrophoresis (SDS-PAGE) was used to further determine the electrophoresis profile of RBCM-NW-G and RBCM, according to a previous study [39].

2.7. Light-heat curve

AuAg, NW-G, RBCM-NW-G (0.1 mg/mL, 2 mL) were irradiated under NIR (808 nm, 2 w/cm^2) at a distance of 20 cm for 1000 s, and the temperature of samples was recorded. The photothermal conversion efficiency of AuAg, NW, and RBCM-NW-G was calculated according to the method reported by Espinosa et al. [40] (Fig. S2, Supporting information).

The temperature changes of RBCM-NW-G with different concentrations (25, 50, 100 and 200 μg/mL) and irradiated with different intensity of NIR (1, 1.5 and 2 w/cm^2) were recorded in a similar way. To test the stability, temperature was recorded on RBCM-NW-G which has been irradiated for 7 times.

2.8. Releasing of GM by RBCM-NW-G

Ten min after preparation of RBCM-NW-G dispersion (100 μg/mL, 1 mL), the dispersions were irradiated with NIR (808 nm, 1.5 w/cm^2) for 0, 5, 10, 15, 20, 25, 30, 35, 40, 45 and 50 min. Then, the dispersion was centrifuged to collect the supernatant, which was used for determination of content of released GM content using ultrahigh performance liquid chromatography (HPLC) (Method S1 and Fig. S3, Supporting information). As a comparison, the contents of released GM in RBCM-NW-G dispersion without irradiation was also measured as a control.

2.9. Releasing of silver ion (Ag^+) by RBCM-NW-G

RBCM-NW-G dispersion (100 μg/mL, 3 mL) were irradiated with NIR (808 nm, 1.5 w/cm^2) for 10, 20, 30, 40 and 50 min. After that the dispersion was centrifuged to collect the supernatant, which was used for determination of content of Ag^+ using inductively coupled plasma mass spectrometry. As a comparison, the content of released Ag^+ in a control group without irradiation was also measured.

2.10. Antibacterial test

S. aureus and *E. coli* were used as the probe bacteria to test the antibacterial properties in vitro. AuAg and RBCM-NW-G nanoparticles were suspended separately in lysogeny broth medium at different concentrations (12.5, 25, 50, 75 and 100 μg/mL). Then, 1 mL of bacteria (OD_{600} = 0.8) was centrifuged and resuspended in 1 mL of medium containing nanoparticles. The cells were then irradiated with NIR (808 nm, 1.5 w/cm^2) for 15 min and incubated at 37 °C for 8 h. The bacteria added with nanoparticles but not the irradiated NIR group, and untreated bacteria were used as controls. Finally, absorbance was measured at 600 nm, and the above-mentioned bacterial dispersion was diluted 10^3 times, 200 μL were taken, spread evenly on the solid medium, and cultivated for 10 h.

2.11. Live/dead bacterial staining assay

Bacteria were treated in the same way as above and irradiated with NIR (808 nm, 1.5 w/cm^2) for 15 min; STYO9 and PI were used to stain and label the bacteria, and observations were made under a fluorescence

microscope.

2.12. Observation of bacterial morphology

Centrifugally collected bacteria treated as above were washed 3 times with phosphate-buffered saline (PBS), then fixed with glutaraldehyde (2.5% fixed for 12 h), and dehydrated with an alcohol gradient (30, 50, 70, 90 and 100%) for 10 min each. The fixed bacteria were observed by SEM and TEM.

2.13. Anti-biofilm activity

S. aureus and *E. coli* (1×10^7 CFU/mL, 1 mL) was added to a 24-well plate with round cover slips at the bottom, and incubated at 37 °C for 48 h, during which the medium was changed after every 12 h. After the biofilm was formed, free bacteria were washed away with PBS, then AuAg and RBCM-NW-G dispersed in the culture medium (100 μg/mL, 1 mL) were added; a control added with culture medium only was set for comparison. The biofilms containing AuAg and RBCM-NW-G were divided into 4 groups: AuAg(−), AuAg(+), RBCM-NW-G(−), and RBCM-NW-G(+). AuAg(+) and RBCM-NW-G(+) were irradiated with 15 min NIR (808 nm, 1.5 w/cm^2), while AuAg(−) and RBCM-NW-G(−) were not. Next, the 4 groups were incubated (37 °C, 1 h), and washed 3 times with PBS. Observations were made using confocal laser scanning microscopy (CLSM), after the biofilm was stained and labeled with STYO9 and PI, and SEM following similar pretreatment for as described in Section 2.12.

2.14. In vitro hemolysis test

Fresh blood from BALB/c mice was used for hemolysis determination. 10 mL of blood containing 1 mL of sodium citrate (3.8%) were centrifuged (2500 rpm, 4 °C) for 5 min to remove serum and obtain fresh RBCs. RBCs was washed three times with PBS and diluted with PBS to obtain a 4% Red blood cells (RBCs) suspension. Then, 1 mL of red blood cell suspension was added to RBCM-NW-G (25, 50, 75, 100, 150 and 200 μg/mL, 1 mL) dispersed in PBS. In addition, 1 mL of red blood cell suspension mixed with 1 mL PBS was used as a positive control, and 1 mL of red blood cell suspension mixed with 1 mL of distilled water was used as a negative control, and the treatment for each sample was repeated 3 times. All samples were incubated at 37 °C with shaking for 45 min, and then centrifuged to detect the absorbance of different samples at 540 nm. Hemolysis ratio was calculated according to Equation (1):

$$\text{Hemolysis ratio } (\%) = (A_2\text{-}A_0) / (A_1\text{-}A_0) \quad (1)$$

where A_2 represents the absorbance of the supernatant after culture mixing of red blood cells and RBCM-NW-G, A_0 is the absorbance of the supernatant after culture mixing of red blood cells and PBS, and A_1 is the absorbance of the supernatant after culture mixing of red blood cells and pure water.

2.15. Biological toxicity

The in vitro cytotoxicity of RBCM-NW-G was evaluated using the MTT assay and LIVE/DEAD Cell Imaging Kit. First, L929 cells (1×10^5 cells/well) were seeded into a 96-well plate and then incubated in 100 μL DMEM containing 10% FBS and 1% antibiotic antimycotic for 24 h at 37 °C prior to sample addition. Then, RBCM-NW-G was added (25, 50, 75, 100, 150 and 200 μg/mL, 50 μL). After incubation for 24, 48, or 72 h, MTT solution (10 μL) and formazan crystals (10 μL) were added to each well. Finally, a microplate reader was used (iMark; Bio-Rad, Hercules, CA, USA) to detect the absorbance of each well at 450 nm.

According to the MTT test results, RBCM-NW-G dispersion (50 μg/mL) was used for live/dead cell imaging. We added 0.5 mL of L929 cells (1×10^5 cells/well) to each well of 24-well plates, and then added RBCM-NW-G dispersion (100 μg/mL, 50 μL) to each well. After incubation for 24, 48, or 72 h, the medium was removed and PBS (1 mL), PI (5 μL), and CalceinAM (15 μL) were added. After incubation at 37 °C for 20 min in the dark, the cell fluorescence was viewed under a microscope (Nikon Ti-E).

To evaluate the safety of RBCM-NW-G to mouse organs. Liver toxicity was assessed by the serum liver enzyme alanine aminotransferase (ALT) and aspartate aminotransferase (AST) concentrations. In addition, histological analysis of the hearts, livers, spleens, lungs, and kidneys were also performed. The RBCM-NW-G was injected into mouse (dosage: 2 mg/kg) for three consecutive days. The control group was injected with saline in the same way. On the 7th and 15th days, the mouse heart blood was taken to determine the content of ALT and AST. On the 15th day, the mice were euthanized, and the heart, liver, spleen, lung, and kidney were taken for histological analysis.

2.16. Pharmacokinetic studies

Six male BALB/c mice (6 weeks old, approximately 25 g) were randomly divided into 2 groups. Mice in the first group was injected with NW-G dispersion (100 μg/mL, 200 μL), and in the second group was injected with RBCM-NW-G per mouse (100 μg/mL, 200 μL). After injection, mouse orbital blood was collected after 0, 5, 15, 30, 45 min, and after 1, 6, 12, and 24 h for determination of the content of Au in the blood (Method S2, Supporting information).

2.17. Biodistribution detection

Male BALB/c mice (6 weeks old, approximately 25 g) were anesthetized with pentobarbital, and the hair on the thighs and back was removed. *S.* aureus (1×10^8 CFU/mL, 50 μL) was injected into the right leg muscle of the mice, and the infection caused the formation of an abscess cavity for 48 h. Then, total 6 infected mice were randomly divided into 2 groups. One group was injected with fluorescein-labeled NW-G (100 μg/mL, 100 μL), and the second group was injected with fluorescein-labeled RBCM-NW-G (100 μg/mL, 100 μL). The mice were then subjected to in vivo fluorescence imaging at 1, 3, 6 and 12 h after injection. At 6 h after injection, the mice were euthanized and dissected; the heart, liver, spleen, lung, and kidney were taken for fluorescence imaging.

2.18. In vivo photothermal effect

The mouse infection model was constructed as described in Section 2.17. Then, total 9 mice after infection were randomly divided into 3 groups. Group 1 was injected with PBS (100 μL) as a control, Group 2 was injected with NW-G (100 μg/mL, 100 μL), and Group 3 was injected with RBCM-NW-G (100 μg/mL, 100 μL). At 6 h after injection, NIR (808 nm, 1.5 w/cm^2) was used to irradiate the infected area, and an infrared thermal camera was used to record the temperature of the infected area.

2.19. In vivo infection animal models

Six mice were randomly equally divided into 2 groups, which were injected with GM (0.0223 mg/kg), and RBCM-NW-G (2 mg/kg) and irradiated with NIR for 30 min/day in 3 consecutive days. Then the infected sites were photographed at the predetermined days. The mice were euthanized on the 7th and 15th days after treatment, the infected part was taken and preserved with formalin before its sections were stained for observation.

3. Results and discussion

3.1. Characterization

AuAg, NW, and RBCM have corresponding plasmon resonance peaks. Therefore, the plasmon resonance peaks of different nanoparticles were detected by UV–vis spectroscopy. As shown in Fig. 2A, the plasmon resonance peak of AuAg is around 750 nm, and the characteristic peak of RBCM is around 420 nm. After wrapping the PDA, the related UV absorption peak shifted to 800 nm. In addition to the NW absorption peak of AuAg at around 800 nm, RBCM-NW-G has an absorption peak of RBCM at around 420 nm, proving the successful encapsulation of the RBCM. Moreover, the surface potential of the particles also changed notably after coating. Fig. 2B shows that the potential of the AuAg was about −30 mV, and the potential of the GM was about +10 mV, which facilitated the GM to fill into the AuAg by electrostatic adsorption. The overall loading percentage of GM in RBCM-NW-G was 11.16%, and the encapsulation ratio was 22.3% (calculated according to Methods S3, Supporting Information). The wrapping of RBCM resulted in a decrease in the average zeta potential of NW-G from 13.1 to −22.9 mV. After wrapping with PDA, the particle size of the AuAg increased from 50 nm to 170 nm (Fig. 2C). To verify the successful wrapping of the PDA and RBCM, the morphology, structure, and size of AuAg, NW, and RBCM-NW-G were observed by TEM. AuAg was confirmed to have a hollow structure, and after wrapping with PDA, a PDA film on the surface of AuAg was observed. In addition, RBCM-NW-G showed a thin RBCM film

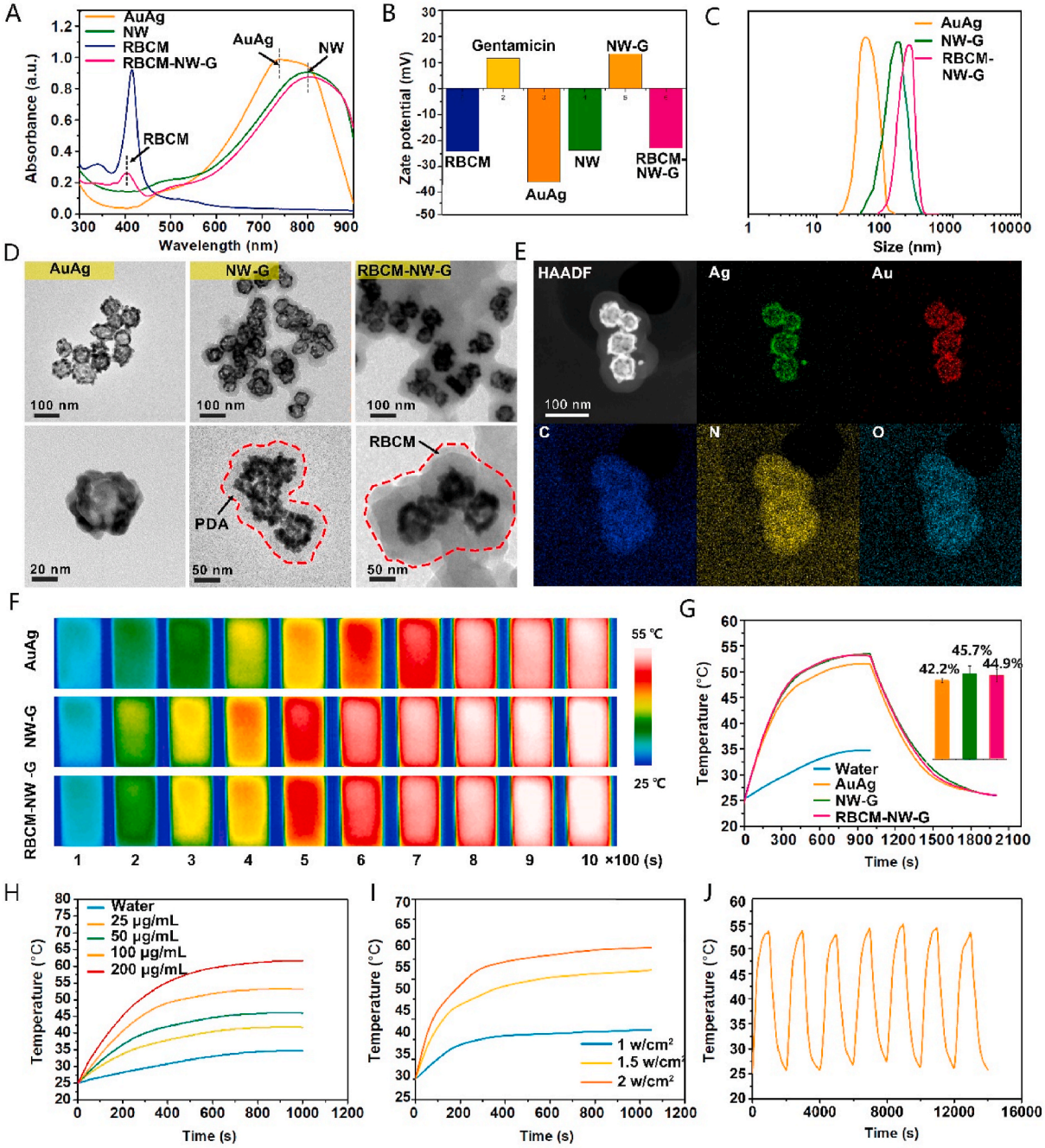

Fig. 2. (A) UV–vis spectra. (B) zeta potentials. (C) Hydrodynamic diameter. (D) TEM images. (E) HAADF-STEM images and elements mapping of RBCM-NW-G. (F) Thermal infrared images. (G) Heating curves and corresponding heat conversion efficiency (inset). (H) Heating curves of RBCM-NW-G with different concentration. (I) Heating curves of RBCM-NW-G under different irradiation intensity. (J) Fatigue test of photothermal effect of RBCM-NW-G in 7 cycles.

on the outer layer of the PDA film (Fig. 2D). As the contrast of PDA and RBCM was quite close, the electrophoresis profiles of RBCM-NW-G and RBCM were further compared (Figure S4, Supporting information). As there was no difference was observed, it could verify the fact that successful package of RBCM over NW-G had been realized [41]. Elemental mapping (Fig. 2E) indicated a uniform distribution of Au and Ag in AuAg, of which the contents in RBCM-NW-G were 1.57% and 2.41% respectively (Fig. S5, Supporting information).

3.2. Observation of the photothermal behavior of RBCM-NW-G

Because AuAg, NW, and RBCM-NW-G have distinct absorption peaks around 800 nm, the photothermal effect of the particles was evaluated by recording the temperature changes under 808 nm NIR irradiation. The temperature changes of AuAg, NW, and RBCM-NW-G were recorded for 1000 s (Fig. 2F and G). The temperature of AuAg, NW, and RBCM-NW-G increased rapidly over time. Notably, the temperature rise of NW-G and RBCM-NW-G was notably faster than that of AuAg. The temperature of AuAg rose from 25 °C to about 51 °C within 1000 s of NIR irradiation, and the photothermal conversion efficiency was 42.2%. However, when the temperature of NW-G and RBCM-NW-G rose to 53 °C, the photothermal conversion efficiencies were 45.7% and 44.9%, respectively, which was slightly higher than that of AuAg. This may be because PDA wrapping increases the photothermal conversion efficiency [42]. However, the temperature of water increased only slightly under NIR irradiation. This demonstrated that the increased temperature in AuAg, NW, and RBCM-NW-G solutions was mainly due to the photothermal effect of the nanoparticles. Next, the effect of the nanoparticle concentration on the temperature rise of the material was explored. Fig. 2H shows that as the particle concentration increased, the temperature rose faster, and the final temperature reached also increased. When the concentration was greater than 100 μg/mL, the final temperature of RBCM-NW-G reached values as high as 50 °C. This temperature has the ability to sterilize without damaging normal tissues [43,44]. The photothermal effect of particles also depends on the laser density, which in turn, has an important effect on the particle temperature. As shown in Fig. 2I, as the laser power increased, the temperature of RBCM-NW-G also increased significantly. Therefore, in the application process, the particle temperature can be controlled by adjusting the concentration of the particles and the power of the laser. Additionally, the heating and cooling of RBCM-NW-G under seven repeated NIR irradiation cycles were recorded (Fig. 2J). The results show that the photothermal conversion ability of RBCM-NW-G did not decrease after seven NIR excitations, proving the good photothermal stability of RBCM-NW-G. In summary, RBCM-NW-G has good photothermal sterilization potential.

3.3. Antibacterial activity

E. coli and *S. aureus*, which are common bacteria in infections, were

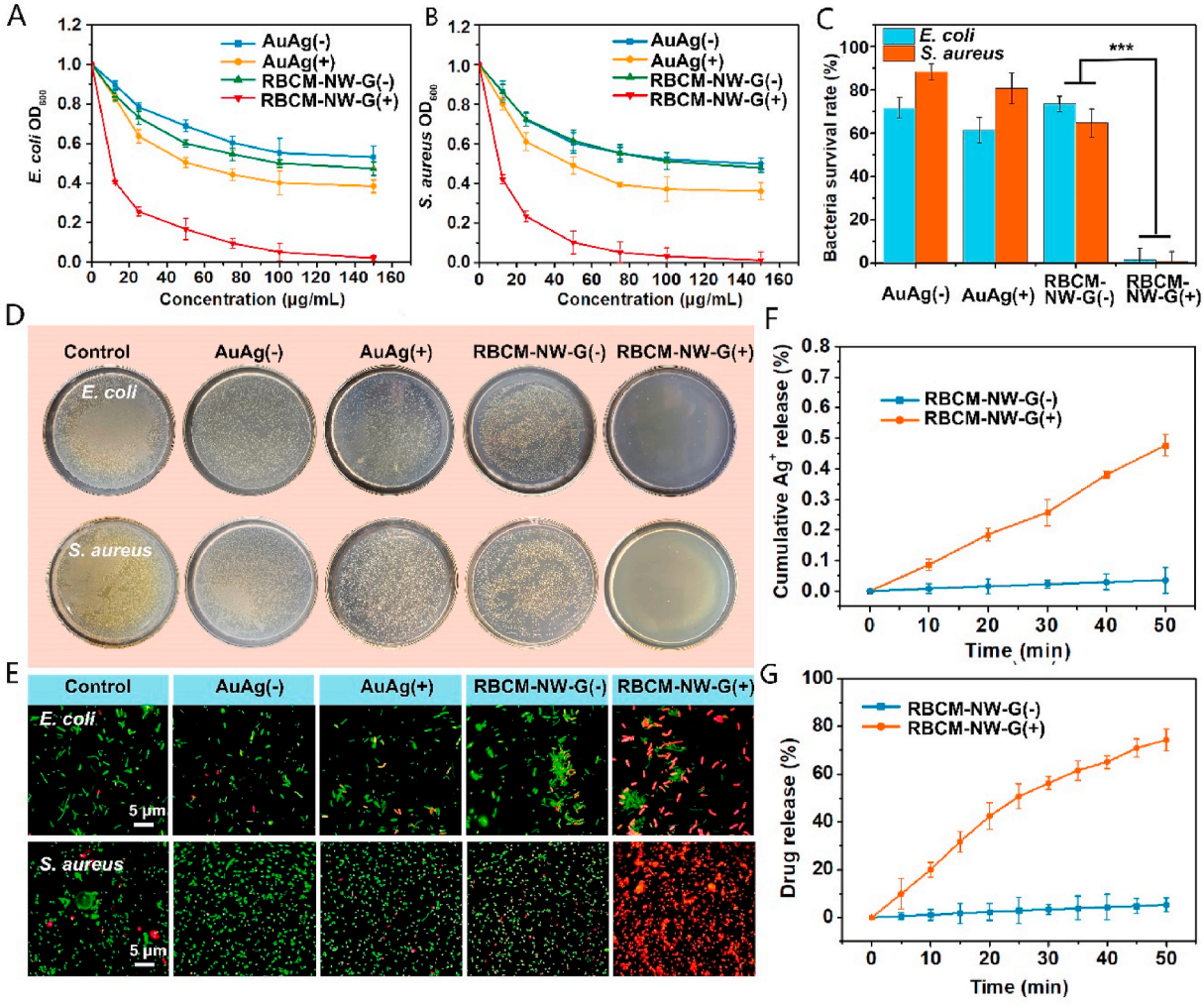

Fig. 3. (A, B) Absorbance of bacterial suspension at 600 nm. (C) Survival rate of bacteria. (D) Photos of bacterial colony. (E) Live/dead fluorescent staining imaging. (F) Ag^{+} released by RBCM-NW-G. (G) GM released by RBCM-NW-G.

used to test the antibacterial properties of the material [45]. The two bacterial strains were cultured with AuAg and RBCM-NW-G with (+)/without (−) NIR irradiation. In addition to observing the bacterial suspension turbidity, the absorbance at the OD600 of the bacterial suspension was measured. As shown in Fig. 3A and B, similar results were obtained for the two bacterial strains. Under NIR irradiation, the antibacterial properties of AuAg and RBCM-NW-G were significantly improved. However, AuAg(+) was not powerful enough to inhibit bacterial growth completely. In contrast, the RBCM-NW-G(+) group showed much higher antibacterial properties than the other three groups. For example, the AuAg(−) group had a bacterial survival rate of 71.7% and 88.4% for *E. coli* and *S. aureus*, respectively, while that of AuAg(+) was 61.4% and 80.7%, respectively. The survival rate in the RBCM-NW-G(−) group was 73.5% and 64.8% for *E. coli* and *S. aureus*, respectively. Surprisingly, the survival rate of bacteria in the RBCM-NW-G(+) group was only 1.6% and 0.9%, respectively (Fig. 3C), which is consistent with the results shown in Fig. 3D. This can be ascribed to the fact that GM from RBCM-NW-G, accounting for loading percentage of 11.16% (Fig. S5, Supporting information), was released by NIR radiation to eliminate bacteria.

Subsequently, the structural integrity of the bacteria was evaluated by live/dead fluorescent staining assays. Bacteria were stained with two fluorescent nucleic acid dyes. SYTO 9 marks all bacteria to show green fluorescence under a fluorescence microscope, while PI only marks dead bacteria to show red fluorescence. Consistent with the previous results, only a small amount of red fluorescence was observed in the control, AuAg(−), AuAg(+), and RBCM-NW-G(−) groups of the two bacterial strains. The red fluorescence of the RBCM-NW-G(+) group was significantly increased (Fig. 3E), proving that RBCM-NW-G(+) effectively destroyed the morphology of the bacteria.

The above results show that the antibacterial properties of RBCM-NW-G and NW-G on the two bacterial strains under NIR irradiation were higher than those without NIR irradiation. One possible reason for this pattern may be that the increased temperature caused by NIR irradiation has led to the release of GM. To validate this probability, contents of released GM during NIR irradiation were measured. As shown in Fig. 3G, GM loaded on RBCM-NW-G could be released under NIR irradiation fast, corresponding to about 30% in 15 min. In addition to the important role of GM, release of Ag^+ from RBCM-NW-G may be another reason. It was noted that, along with the release of GM, Ag^+ could be released under NIR irradiation as well, although the releasing percentage was ultralow (Fig. 3F). Therefore, the high antibacterial performance of RBCM-NW-G may be due to the synergy of the photothermal effect, Ag^+, and antibiotics.

3.4. Morphological observation of bacteria

The bacterial morphology after treatment under different conditions was observed by SEM. Fig. 4A shows that *E. coli* and *S. aureus* both had a smooth surface and a complete rod-like or spherical structure before being treated. After treatment with AuAg(−), AuAg(+), and RBCM-NW-G(−), both bacterial strains were slightly damaged, and the edges of the bacteria became rough. However, the morphological structure of the bacteria was still complete. However, after RBCM-NW-G(+) treatment, the morphology of the bacteria was seriously disrupted. Bacterial cell walls were lysed, and the shape of the bacteria changed. The cell membrane was destroyed and the endoplasm of the cells flew out. In addition, a large number of nanoparticle aggregations was observed on the bacterial surface in the RBCM-NW-G(−) and RBCM-NW-G(+) groups.

These phenomena were more evident in the TEM images. As shown in Fig. 4B, the untreated *S. aureus* and *E. coli* had a clear outline, and the internal structure of the cell was complete. After RBCM-NW-G culture and NIR excitation, both *S. aureus* and *E. coli* were killed in large numbers, the bacteria were lysed, and the intracellular material was dissolved. It is worth noting that a pronounced RBCM-NW-G particle aggregation was observed around the dead bacteria, which is beneficial for increasing the concentration of Ag^+ and antibiotics around the bacteria to improve the sterilization efficiency.

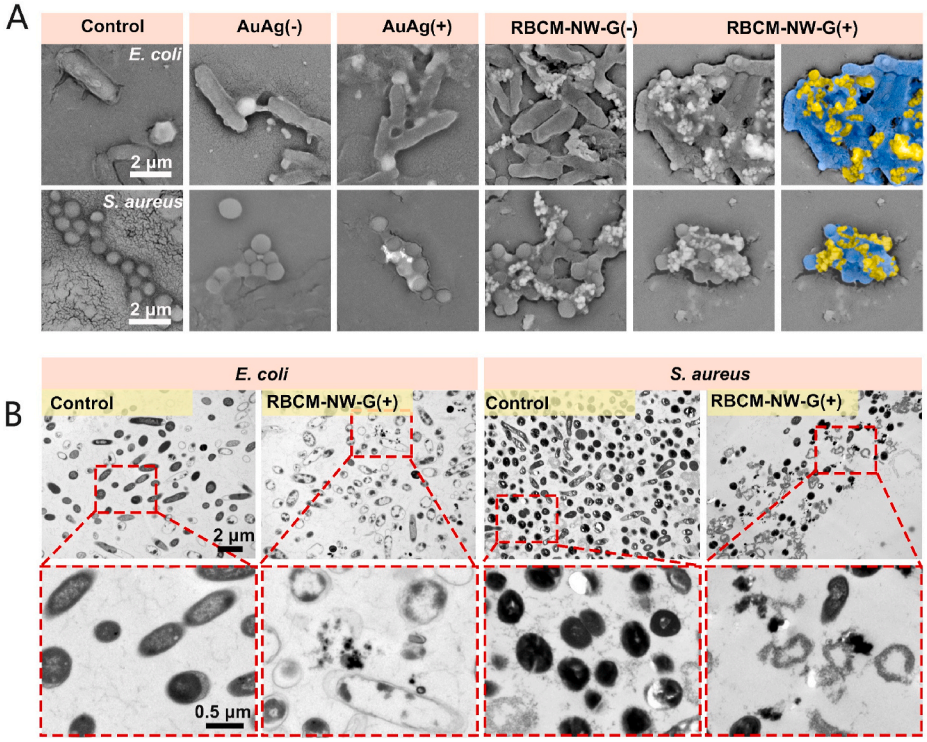

Fig. 4. (A) SEM images of bacteria. (B) TEM images of bacteria.

3.5. Antibiofilm activity of RBCM-NW-G nanoparticles in vitro

The existence of a biofilm hinders the effective penetration of antibiotics and affects their therapeutic effect [46,47]. Therefore, whether the particles can effectively penetrate the biofilm is key to the determination of the therapeutic effect. Here, the bactericidal effects of AuAg and RBCM-NW-G with/without NIR excitation conditions on *S. aureus* and *E. coli* biofilms were systematically tested. To visually observe the morphological changes of biofilm bacteria, the antibacterial ability of RBCM-NW-G was qualitatively analyzed using SEM. As shown in Fig. 5A, the biofilm structure of the control group was complete and compact, and the bacteria had a clear morphology and complete structure. After culturing with RBCM-NW-G, many RBCM-NW-G particles accumulated on the surface of the biofilm. In the RBCM-NW-G(−) group, although RBCM-NW-G was tightly bound to the surface of the biofilm, the bacteria still had an intact morphology. However, after irradiation with NIR, the biofilm was destroyed, and the bacteria twisted and lysed, proving the good antibacterial properties of RBCM-NW-G.

Furthermore, Live/dead staining was used to detect the survival status of the bacteria in the biofilms. The antibacterial effects of AuAg and RBCM-NW-G with/without NIR excitation were photographed using CLSM. Fig. 5B and C shows that without NIR excitation, AuAg and RBCM-NW-G group can only observe hardly red fluorescence on the surface of the biofilm and higher relative fluorescence intensity, suggesting there is almost no bactericidal effect. In contrast, the RBCM-NW-G(+) group showed the lowest relative fluorescence intensity, where most areas fluoresced red, and even the bacteria on the bottom were killed. Taken together, the destruction of the biofilm by the photothermal effect enabled the nanoparticles to effectively penetrate into the bacteria in the biofilm, and the combined action of the photothermal effect and antibiotics showed an efficient sterilization ability.

3.6. In vivo biodistribution study

Extending the retention time of particles in blood during blood circulation is an important way to improve the efficiency of antibiotics [44]. Therefore, to test whether the RBCM in RBCM-NW-G retains a long circulation time, a pharmacokinetic study of RBCM-NW-G was conducted using a mouse model. The results showed that RBCM-NW-G significantly enhanced circulation time. As shown in Fig. 6A, the blood retention of NW-G was only 3.1% ID/g, while that of RBCM-NW-G was as high as 14.4% ID/g after 12 h. Even after 24 h, RBCM-NW-G still preserved 13.1% ID/g, which was 11.6% ID/g higher than that of NW-G. This proves that RBCM-NW-G nanoparticles had successfully been endowed with long blood circulation time characteristics, which further improves the efficient use and avoids the abuse of antibiotics. To further explore the distribution of RBCM-NW-G in organisms, a mouse model of infection was used to conduct bioimaging analysis. Fig. 6B and D shows that the fluorescence in the NW-G group distributed rapidly, but there was no noticeable accumulation at the infection site. In addition, the fluorescence gradually weakened over time, and only a weak fluorescence signal appeared around the heart at 12 h. The fluorescence distribution of the RBCM-NW-G group was significantly different from that of NW-G. One hour after injection, a tendency of RBCM-NW-G to accumulate at the infected site was observed. The fluorescence of other organs in the mouse gradually decreased over time, while the fluorescence of the infected site gradually increased. After 6 h, the fluorescence intensity of the RBCM-NW-G group was 4 times that of the NW-G group.

Fig. 6D shows the distribution of nanoparticles in living mice, while Figure C and E show the distribution in different organs of mice. Similarly, a strong fluorescence was observed in the infected muscle of the RBCM-NW-G group, while an only weak fluorescence was observed in the infected muscle of the NW-G group. This demonstrates that camouflaging the RBCM not only increased the blood circulation time of the RBCM-NW-G nanoparticles, but also enabled them to effectively accumulate at the infected site. This may be a synergistic effect of the

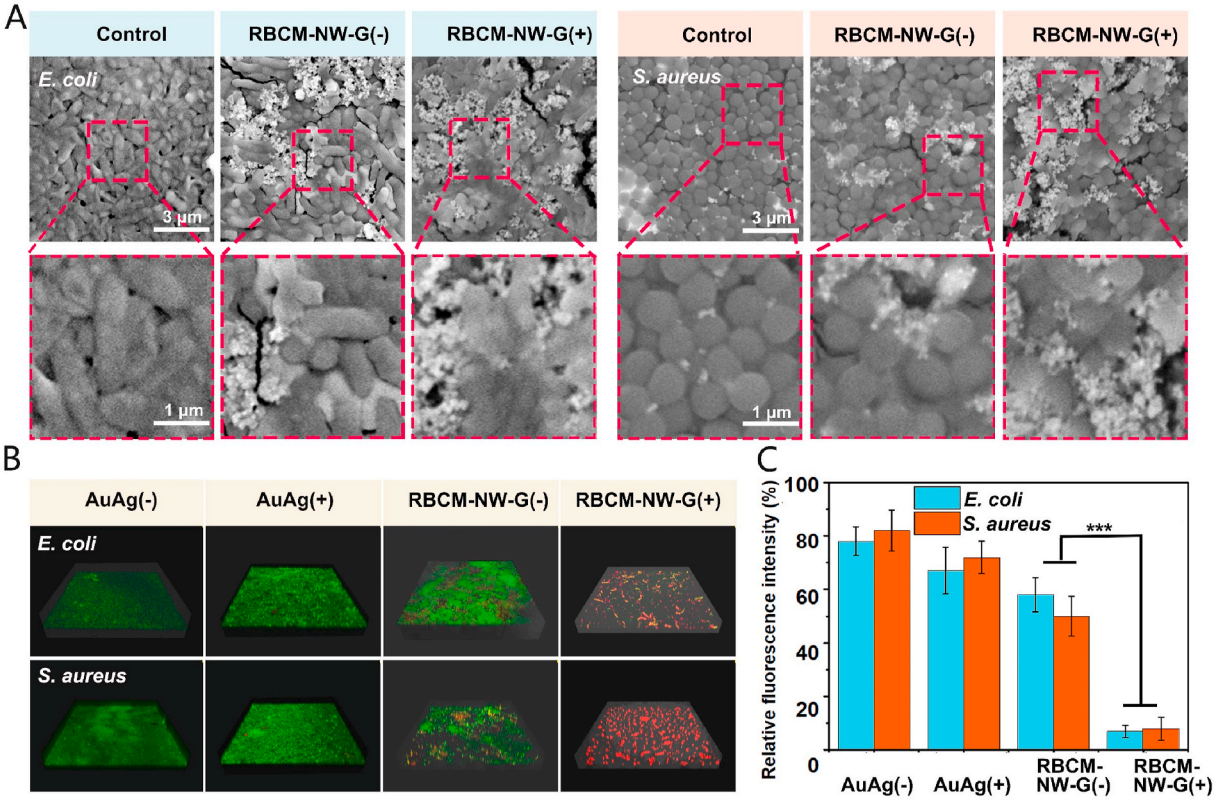

Fig. 5. (A) SEM images of bacterial biofilms. (B) CLSM imaging of bacterial biofilms. (C) Relative fluorescence intensity of bacterial biofilms.

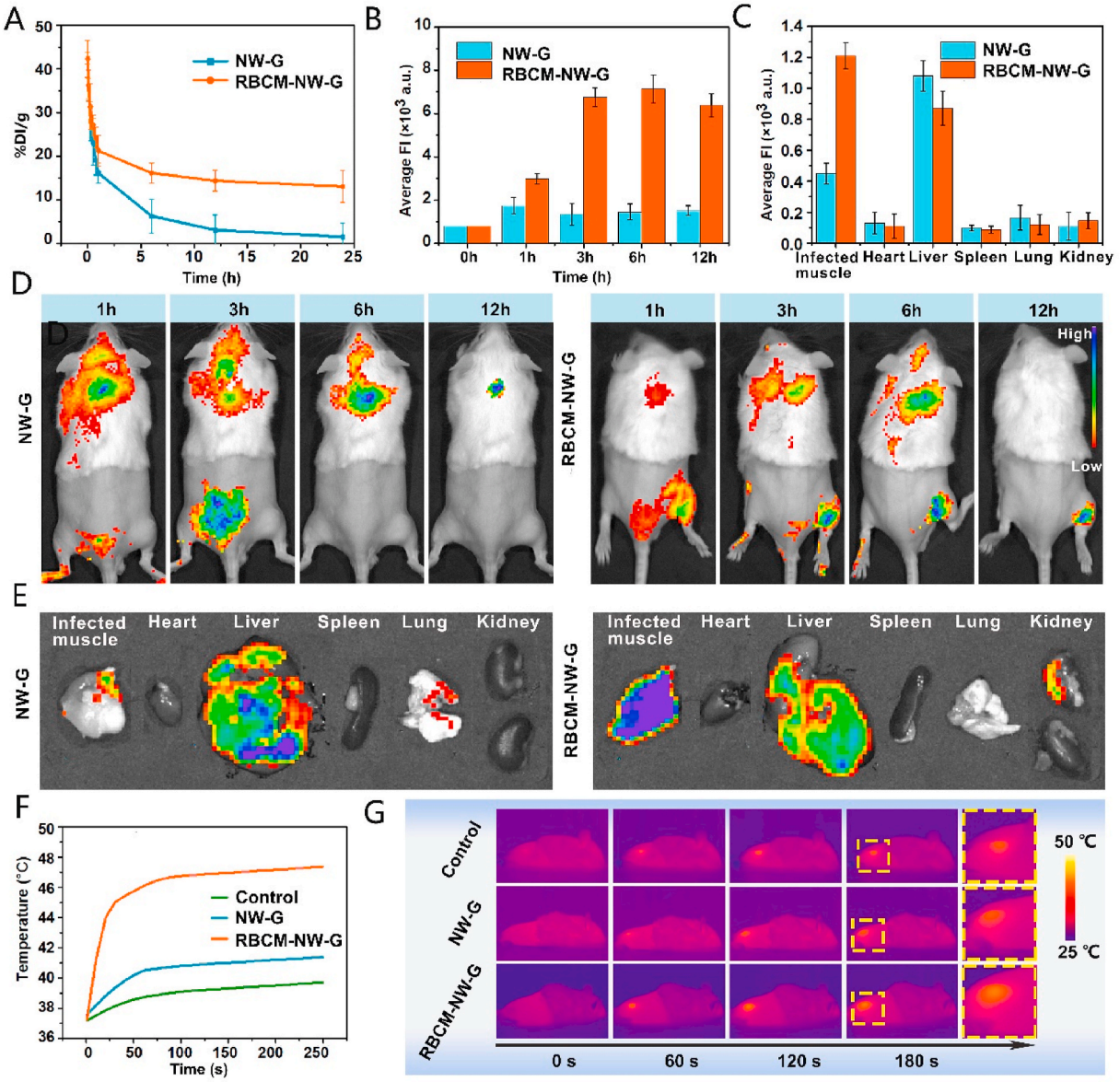

Fig. 6. (A) Retention of NW-G and RBCM-NW-G in blood. (B) Relative fluorescence intensity in mice. (C) Relative fluorescence intensity in infected muscle and organs at 6 h. (D) Fluorescence distribution in living mice. (E) Fluorescence distribution in infected muscle and organs of dissected mice at 6 h. (F) Heating curves of the infected muscle. (G) Near-infrared imaging of the infected muscle.

immune escape and EPR effects at the infection site [48,49].

In the antibacterial part, the PT was confirmed to promote the penetration of the RBCM-NW-G particles into bacterial biofilms. Therefore, thermal imaging equipment was used to evaluate the photothermal effect in vivo. Fig. 6F and G shows that under NIR irradiation, the three groups of mice showed clear temperature changes at the infected site. Among them, the temperature of the PBS group increased slightly under NIR irradiation. The NW-G temperature rose faster than that in the PBS group, and the final temperature was higher. Surprisingly, the temperature of the RBCM-NW-G group was significantly higher than that of the other groups, showing a good photothermal effect. When the RBCM-NW-G group was irradiated with NIR for 90 s, the temperature had already reached 45 °C. The final temperature was 7 °C higher than that of the NW-G group.

3.7. *In vivo infection treatment testing*

Subsequently, a mouse leg infection model was established to test the therapeutic effect of RBCM-NW-G nanoparticles in actual infections. As shown in Fig. 7A and B, a small number of bacteria were present in the infected muscle of the mice after infection. After treatment with a single injection of antibiotics, the infection site became larger and the number of bacteria increased significantly.

Fig. 7C and D shows that RBCM-NW-G(+) had a good antibacterial effect. After the treatment, the infection site of the mice gradually decreased over time. The number of bacteria also gradually decreased, whether it was on 7 day or 15 day, and the number of bacteria was much smaller than that of the control group (Figure S6A, Supporting information). Notably, the infected muscle of the mice in the RBCM-NW-G(+) group recovered almost completely after 15 days. This proves that the antibiotics used alone were not capable of inhibiting the bacteria at the infection site. However, RBCM-NW-G had a good inhibitory effect on the bacteria at the infection site under NIR excitation.

As shown in Fig. 7E and F, the infected sites of the three mice in the GM group swelled over time. The abscess in the mice in the RBCM-NW-G (+) group showed a decreasing trend as time increased (Fig. S6B,

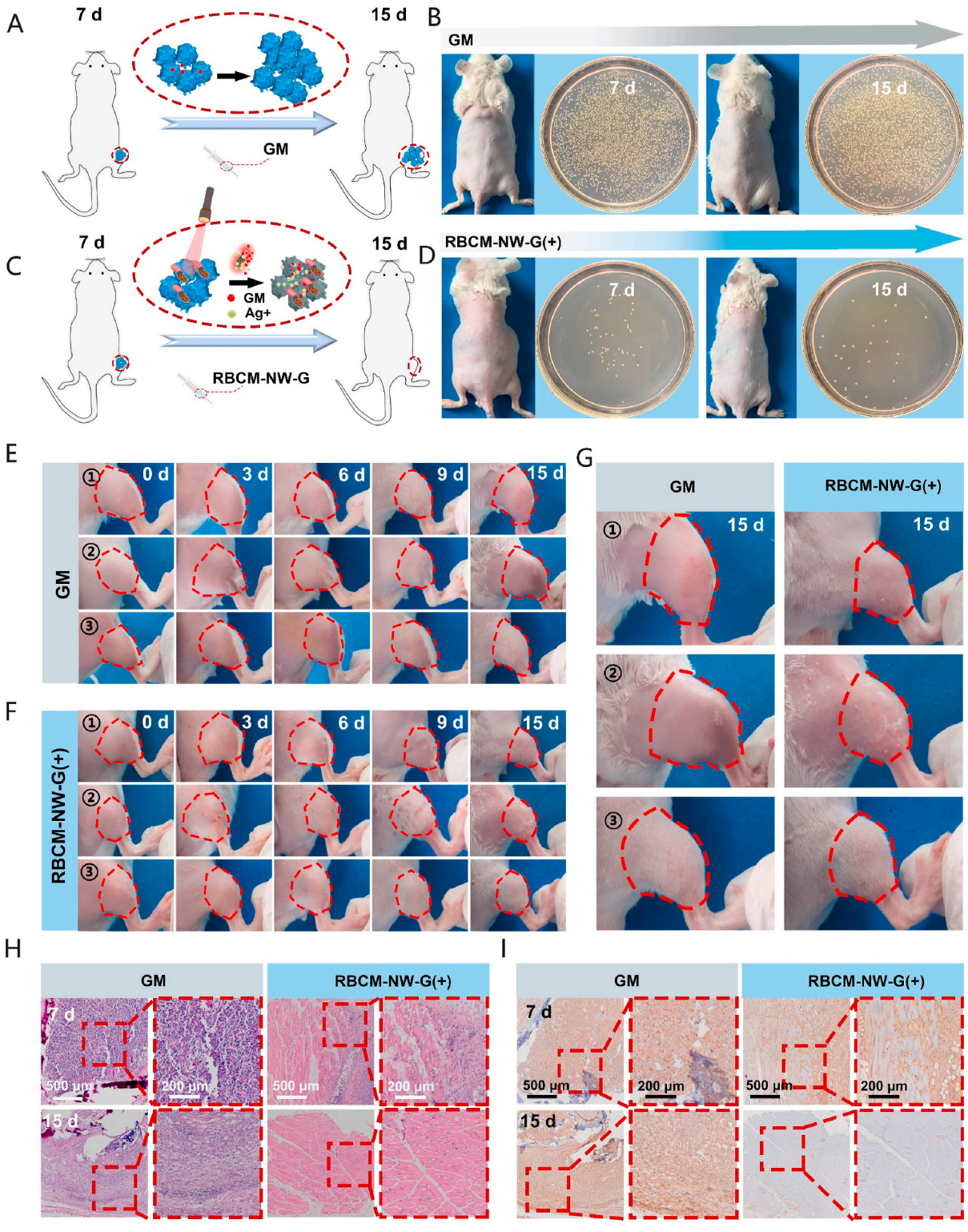

Fig. 7. (A, B) Diagram of treating mice. (C, D) Photo of mice and the related colonies in infected areas. (E, F) Photos of infected parts of mice at different days. (G) Magnified photos of infected parts of mice on day 15. (H, I) H&E and CD68 staining of the infected site of mice.

Supporting information). On day 15, the infected site of the mice in the GM group was severely swollen, while the swelling of the infected site of the mice in the RBCM-NW-G(+) group was eliminated (Fig. 7G). In addition, histological analysis of the infected tissues was performed by H&E and CD-68 staining. As shown in Fig. 7H and I, on day 7, a large number of inflammatory cells, such as macrophages and neutrophils, was observed in the GM group. Although there were some inflammatory cells in the RBCM-NW-G(+) group, they were much less than in the GM group (Fig. S6C & D). On day 15, the infection in the RBCM-NW-G(+) group was almost eliminated and no marked inflammation was observed. However, there was still a large number of inflammatory cells in the GM group. In summary, the above tissue analysis shows that

RBCM-NW-G(+) had a good therapeutic effect on bacterial infections in vivo.

3.8. Cytotoxicity

RBCM-NW-G is transported through blood, so that it is necessary to ensure that RBCM-NW-G will not impact red blood cells. Here, RBCs of mice were used to test the hemolysis rate of different concentrations of RBCM-NW-G. As shown in Fig. 8A, the hemolysis rate of the highest concentration (200 μg/mL) of RBCM-NW-G was only 3.6%, indicating that RBCM-NW-G did no evident damage to the RBCs. To verify that RBCM-NW-G is a safe material, the biocompatibility of the material was tested with L929 cells. First, we used the MTT method to determine the biocompatibility of different concentrations of RBCM-NW-G. As shown

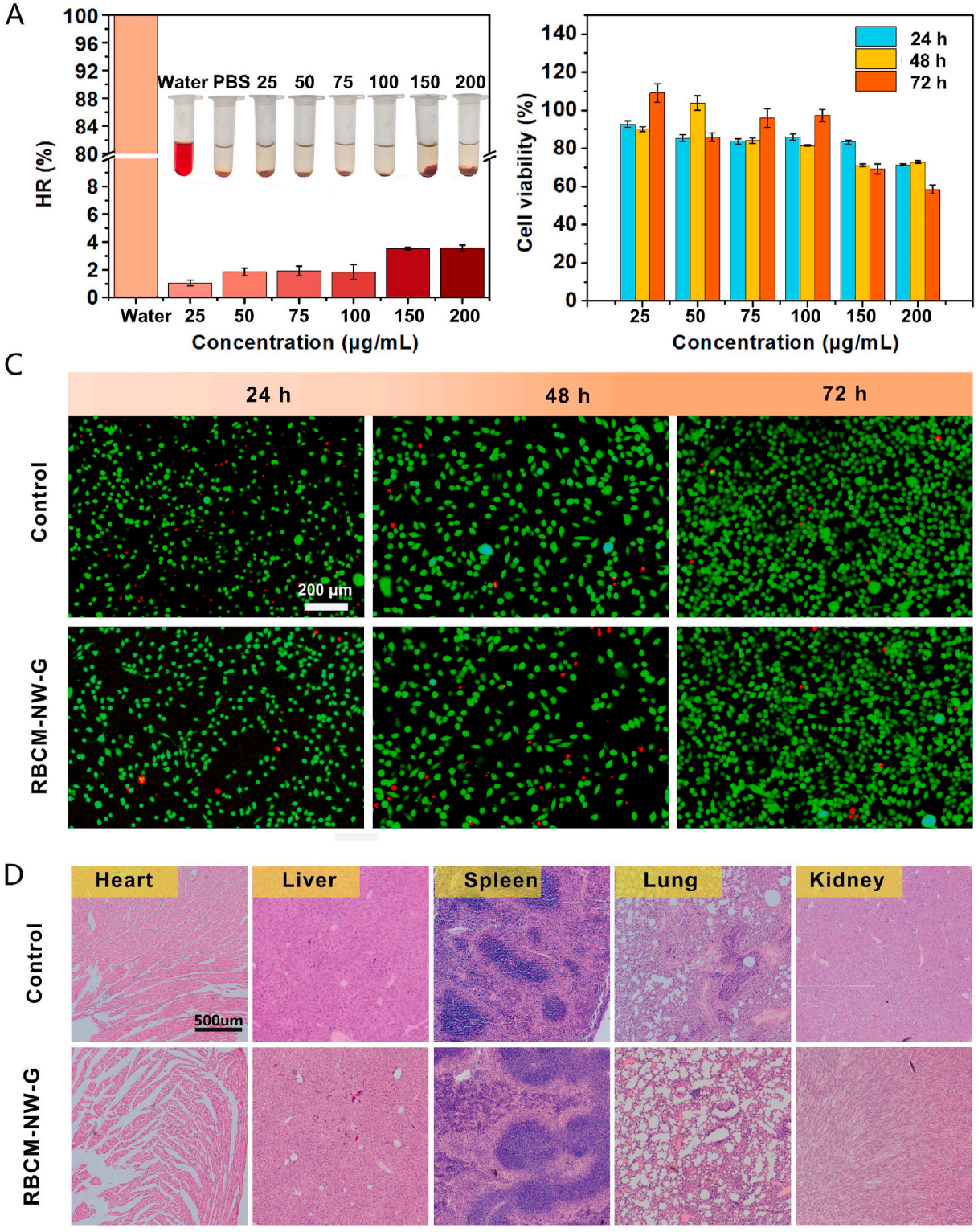

Fig. 8. (A) Survival rate of RBCs cultured with RBCM-NW-G. (B) Survival rate of L929 cells cultured with RBCM-NW-G. (C) Live/dead fluorescent staining imaging. (D) H&E staining of the heart, liver, spleen, lung, and kidney.

in Fig. 8B, the cell survival rate was greater than 80% when the concentration of RBCM-NW-G was controlled to be lower than 100 μg/mL, indicating that there was no notable toxicity to the L929 cells.

According to the results of MTT assays, RBCM-NW-G at a concentration of 100 μg/mL was used for co-culture with L929 cells, and then, fluorescent labeling and observation were performed. Fig. 8C shows that 24, 48, and 72 h after RBCM-NW-G treatment, the cell morphology was normal, and with an increase in time, the cell density increased. This was consistent with the control group. Similarly, there was only a small amount of red fluorescence in the cells at the three time points, which proves that only a small number of L929 cells were apoptotic. The above results prove that the material did not affect the proliferation of L929 cells, and no notable cytotoxicity was seen.

The liver injury was evaluated by the concentration of ALT and AST. On the 7th and 15th days, the ALT and AST concentrations of the mice injected with RBCM-NW-G were not significantly different from those of the control group, proving that RBCM-NW- G was not toxic to mouse liver (Fig. S7A & B, Supporting information). To detect the effect of RBCM-NW-G on the organs of mice, histological analyses of the hearts, livers, spleens, lungs, and kidneys were performed. As shown in Fig. 8D, on day 15 after the injection of RBCM-NW-G, there was no evident tissue damage in the various organs of the mice compared with the control group. This proved that RBCM-NW-G particles were not potentially toxic to the biological organs.

4. Conclusions

In this study, a new biomimetic nanosystem was successfully developed for the treatment of bacterial infections in vivo, achieving a controllable and efficient use of antibiotics. High-efficiency antibacterial effects have been achieved by combining the photothermal effect, Ag^{+}, and antibiotics for synergistic sterilization, which solves the difficulties antibiotics have in penetrating biofilms. RBCM-NW-G, which retains the immune escape ability of RBCM, not only shows good biocompatibility but also effectively aggregates at the infected site. Through in vitro NIR excitation, the temperature of the nanoparticles increases due to the photothermal effect, thereby releasing antibiotics and Ag^{+}. Local temperature increases destroy the biofilms so that antibiotics and Ag^{+} can penetrate the biofilm to achieve an efficient sterilization. The results of antibacterial experiments and mouse infection models proved that this combined antibacterial strategy can enhance the permeability of antibacterial biofilms to effectively treat bacterial infections in vivo. Taken together, RBCM-NW-G provides a new idea for bacterial biofilm infections and the efficient use of antibiotics. In addition, the excellent drug-carrying performance, optical properties, and biocompatibility of RBCM-NW have great potential in the biomedical field.

CRediT authorship contribution statement

Luoxiao Ran: Investigation, Methodology, Formal analysis, Writing – original draft. **Bitao Lu:** Investigation, Methodology, Formal analysis, Writing – original draft. **Haoyu Qiu:** Formal analysis. **Guofang Zhou:** Data curation. **Jing Jiang:** Validation. **Enling Hu:** Writing – review & editing. **Fangyin Dai:** Funding acquisition. **Guangqian Lan:** Conceptualization.

Declaration of competing interest

The authors declare no conflict of interest.

Acknowledgements

Luoxiao Ran and Bitao Lu contributed equally to this work. This work was supported by the National Natural Science Foundation of China (Nos. 51803170, 51803171 and 81703424), China Agricultural Research System (No. CARS-18-ZJ0102), and Fundamental Research Funds for the Central Universities (2020CDJQY-A041).

Appendix A. Supplementary data

Supplementary data to this article can be found online at https://doi.org/10.1016/j.bioactmat.2021.01.032.

References

[1] H. Luo, et al., Engineering an antibacterial nanofibrous membrane containing N-Halamine for recyclable wound dressing application, Mater. Today Commun. 23 (2020) 100898.
[2] Y. Yu, et al., Multifunctional hydrogel based on ionic liquid with antibacterial performance, J. Mol. Liq. (2020) 299.
[3] S. Wu, et al., Silica-coated gold-silver nanocages as photothermal antibacterial agents for combined anti-infective therapy, ACS Appl. Mater. Interfaces 11 (19) (2019) 17177–17183.
[4] K.E. Boehle, et al., Utilizing paper-based devices for antimicrobial-resistant bacteria detection 56 (24) (2017) 6886–6890.
[5] Charge-switchable polymeric coating kills bacteria and prevents biofilm formation in vivo, ACS Appl. Mater. Interfaces 11 (42) (2019) 39150–39162.
[6] Z. Yuan, et al., Near-infrared light-triggered nitric-oxide-enhanced photodynamic therapy and low-temperature photothermal therapy for biofilm elimination, ACS Nano 14 (3) (2020) 3546–3562. XXXX(XXX).
[7] O. Ciofu, T. Tolker-Nielsen, Tolerance and resistance of Pseudomonas aeruginosa biofilms to antimicrobial agents—how P. aeruginosa can escape antibiotics, Front. Microbiol. 10 (2019).
[8] G. Humphreys, F. Fleck, United nations meeting on antimicrobial resistance: world leaders gather at the United Nations general assembly in New York this month to mount a response to the growing threat of antimicrobial resistance, Bull. World Health Organ. 94 (2016).
[9] R. Chen, et al., Antimicrobial peptide melimine coating for titanium and its in vivo antibacterial activity in rodent subcutaneous infection models, Biomaterials 85 (85) (2016) 142–151.
[10] T. Pulingam, et al., Synergistic antibacterial actions of graphene oxide and antibiotics towards bacteria and the toxicological effects of graphene oxide on human epidermal keratinocytes, Eur. J. Pharmaceut. Sci. (2020) 142.
[11] C. Heal, et al., Topical antibiotics for preventing surgical site infection in wounds healing by primary intention 11 (11) (2016), 0-0.
[12] H. Sun, et al., Cancer cell membrane-coated gold nanocages with hyperthermia-triggered drug release and homotypic target inhibit growth and metastasis of breast cancer, Adv. Funct. Mater. 27 (3) (2017) 1604300.
[13] L. Feng, et al., Near-infrared upconversion mesoporous tin oxide bio-photocatalyst for H2O2-activatable O2-generating magnetic targeting synergetic treatment, ACS Appl. Mater. Interfaces 12 (37) (2020) 41047–41061. XXXX(XXX).
[14] N. Levi-Polyachenko, et al., Eradicating group A streptococcus bacteria and biofilms using functionalised multi-wall carbon nanotubes, Int. J. Hypertherm. Off. J. Eur. Soc. Hypertherm. Oncol. North Am. Hypertherm. Group 30 (7) (2014) 490–501.
[15] M. Kim, J. Lee, J.i. Nam, Plasmonic photothermal nanoparticles for biomedical applications, Adv. Sci. (2019) 1900471.
[16] C. Tong, et al., PB@PDA@Ag nanosystem for synergistically eradicating MRSA and accelerating diabetic wound healing assisted with laser irradiation, Biomaterials 243 (2020) 119936.
[17] Gao, et al., Near-infrared light-controllable on-demand antibiotics release using thermo-sensitive hydrogel-based drug reservoir for combating bacterial infection, Biomaterials 188 (2018) 83–95.
[18] Y. Qiao, et al., Near-infrared laser-excited nanoparticles to eradicate multidrug-resistant bacteria and promote wound healing, ACS Appl. Mater. Interfaces (2017) 193–206.
[19] N. Xu, et al., Apoptotic cell-mimicking gold nanocages loaded with LXR agonist for attenuating the progression of murine systemic lupus erythematosus, Biomaterials 198 (2019) 380–392.
[20] Z. Zhang, et al., Near-infrared triggered co-delivery of doxorubicin and quercetin by using gold nanocages with tetradecanol to maximize anti-tumor effects on MCF-7/ADR cells, J. Colloid Interface Sci. 509 (2018) 47–57.
[21] Y. Feng, et al., Time-staggered delivery of erlotinib and doxorubicin by gold nanocages with two smart polymers for reprogrammable release and synergistic with photothermal therapy, Biomaterials 217 (2019) 119327.
[22] M. Li, et al., NIR-Activated polydopamine-coated carrier-free "nanobomb" for in situ on-demand drug release, Adv. Sci. (2018) 1800155.
[23] Li Sen , et al. , , Multifunctional Fe?O?@polydopamine core-shell nanocomposites for intracellular mRNA detection and imaging-guided photothermal therapy, ACS Nano 8 (4) (2014) 3876–3883.
[24] W.F.J.N.M. Liu, Control by Cell Size, vol. 17, 2018, pp. 1055–1056, 12.
[25] X. Wang, et al., Multi-responsive photothermal-chemotherapy with drug-loaded melanin-like nanoparticles for synergetic tumor ablation, Biomaterials 81 (2016) 114–124.
[26] X. Wang, et al., A polydopamine nanoparticle knotted poly(ethylene glycol) hydrogel for on-demand drug delivery and chemo-photothermal therapy, Chem. Mater. 29 (3) (2017) 1370–1376.

[27] E. Moazzen, et al., A novel biocompatible drug carrier for oral delivery and controlled release of antibiotic drug: loading and release of clarithromycin as an antibiotic drug model 66 (2) (2013) 345–351.
[28] Torchilin, P. Vladimir, Multifunctional, stimuli-sensitive nanoparticulate systems for drug delivery, Nat. Rev. Drug Discov. 13 (11) (2014) 813–827.
[29] Q. Pei, et al., Light-activatable red blood cell membrane-camouflaged dimeric prodrug nanoparticles for synergistic photodynamic/chemotherapy, ACS Nano 12 (2) (2018).
[30] C. Wang, et al., Pretreated macrophage-membrane-coated gold nanocages for precise drug delivery for treatment of bacterial infections, Adv. Mater. 30 (46) (2018), e1804023.
[31] M. Xuan, et al., Macrophage cell membrane camouflaged mesoporous silica nanocapsules for in vivo cancer therapy, Adv. Healthc. Mater. 4 (11) (2015), 1578-1578.
[32] M. Ying, et al., Remote-Loaded Platelet Vesicles for Disease-targeted Delivery of Therapeutics, Other, 2018, 28(22).
[33] S. Ye, et al., Light/pH-triggered biomimetic red blood cell membranes camouflaged small molecular drug assemblies for imaging-guided combinational chemo-photothermal therapy, ACS Appl. Mater. Interfaces 11 (17) (2019).
[34] H. Sun, et al., Cancer-cell-biomimetic nanoparticles for targeted therapy of homotypic tumors, Adv. Mater. 28 (43) (2016) 9581.
[35] G. Wan, et al., Nanoscaled red blood cells facilitate breast cancer treatment by combining photothermal/photodynamic therapy and chemotherapy, Biomaterials 161 (2018) 25–40.
[36] C.M.J. Hu, et al., Erythrocyte membrane-camouflaged polymeric nanoparticles as a biomimetic delivery platform, Proc. Natl. Acad. Sci. U.S.A. 108 (27) (2011) 10980–10985.
[37] Z. Liu, et al., Fabrication of red blood cell membrane-camouflaged Cu2−xSe nanoparticles for phototherapy in the second near-infrared window, Chem. Commun. 55 (2019).
[38] A. Lin, et al., Bacteria-Responsive biomimetic selenium nanosystem for multidrug-resistant bacterial infection detection and inhibition, ACS Nano 13 (12) (2019) 13965–13984.
[39] D. Zheng, et al., RBC membrane camouflaged semiconducting polymer nanoparticles for near-infrared photoacoustic imaging and photothermal therapy 12 (1) (2020) 1–17.
[40] A. Espinosa, et al., Janus magnetic-plasmonic nanoparticles for magnetically guided and thermally activated cancer therapy, Small 16 (11) (2020).
[41] D. Zheng, et al., RBC membrane camouflaged semiconducting polymer nanoparticles for near-infrared photoacoustic imaging and photothermal therapy, Nano-Micro Lett. 12 (1) (2020) 1–17.
[42] W. Wang, et al., Mussel inspired polydopamine: the bridge for targeting drug delivery system and synergistic cancer treatment, Macromol. Biosci. 20 (10) (2020).
[43] J. Sun, et al., Synergistic photodynamic and photothermal antibacterial nanocomposite membrane triggered by single NIR light source, ACS Appl. Mater. Interfaces 11 (30) (2019).
[44] G. Gao, et al., Near-infrared light-controllable on-demand antibiotics release using thermo-sensitive hydrogel-based drug reservoir for combating bacterial infection, Biomaterials 188 (2019) 83–95.
[45] C. Mao, et al., Photo-inspired antibacterial activity and wound healing acceleration by hydrogel embedded with Ag/Ag@AgCl/ZnO nanostructures, ACS Nano 11 (9) (2017) 9010–9021, acsnano.7b03513.
[46] D. Hu, et al., Surface-adaptive gold nanoparticles with effective adherence and enhanced photothermal ablation of methicillin-resistant Staphylococcus aureus biofilm, ACS Nano 11 (9) (2017) 9330–9339.
[47] P.C. Naha, et al., Dextran-coated iron oxide nanoparticles as biomimetic catalysts for localized and pH-activated biofilm disruption, ACS Nano 13 (5) (2019) 4960–4971.
[48] D. Zheng, et al., RBC membrane camouflaged semiconducting polymer nanoparticles for near-infrared photoacoustic imaging and photothermal therapy, Nano-Micro Lett. 12 (1) (2020).
[49] S. Chen, Y. Ren, P. Duan, Biomimetic nanoparticle loading obatoclax mesylate for the treatment of non-small-cell lung cancer (NSCLC) through suppressing Bcl-2 signaling, Biomed. Pharmacother. (2020) 129.